



## Microstructure and mechanical properties of heat affected zone in multi-pass GMA welded Al–Zn–Mg–Cu alloy

Jia-liang ZHOU<sup>1</sup>, Feng-yuan SHU<sup>1</sup>, Hong-yun ZHAO<sup>1</sup>, Yao-hui LÜ<sup>2</sup>, Yu-xin LIU<sup>2</sup>, Peng HE<sup>3</sup>

1. Shandong Provincial Key Laboratory of Special Welding Technology,

Harbin Institute of Technology at Weihai, Weihai 264209, China;

2. National Key Laboratory of Remanufacturing, Beijing 100072, China;

3. State Key Laboratory of Advanced Welding and Joining, Harbin Institute of Technology, Harbin 150001, China

Received 22 June 2018; accepted 28 November 2018

**Abstract:** Microstructure and mechanical properties of the heat affected zone (HAZ) in multi-pass gas metal arc (GMA) welded Al–Zn–Mg–Cu alloy plates were investigated, based upon which the mechanical anisotropy and fracture mechanism were analyzed. The microstructure and composition were analyzed by scanning electron microscope (SEM) and energy dispersive spectrometer (EDS). X-ray diffractometer (XRD), transmission electron microscope (TEM) and selective area electron diffraction (SAED) were used to analyze the phase composition. The distribution of microhardness was identified as gradual transition and tensile strength had a tendency to decrease first and then increase. The distribution of nano-sized  $\eta$ (MgZn<sub>2</sub>) particles in the  $\alpha$ (Al) matrix and Al<sub>2</sub>MgCu phase determined the tensile performances along the thickness direction and led to the formation of ductile/brittle composite fracture in the HAZ. The continuous distribution of Al<sub>2</sub>MgCu phase in the strip intergranular precipitates gave birth to premature cracks and the brittle fracture region. The precipitated particles coarsening also led to the deterioration of mechanical properties.

**Key words:** Al–Zn–Mg–Cu alloy; heat affected zone; microstructure; mechanical properties; ductile/brittle composite fracture

### 1 Introduction

Al–Zn–Mg–Cu alloys have been widely used in aerospace vehicles, high-speed trains, automobiles, ships, important military facilities and the other industries so as to reduce mass and cost [1,2]. The mechanical performances of the joints are significantly deteriorated by the discount mechanical properties and the low stress corrosion cracking resistance of the HAZ [3], which is similar to that of Al–Cu and Al–Mg alloys [4] and will be attributed to the obvious differences in microstructure between the HAZ and the base metal [5].

Low yield strength and hardness in the HAZ of Al–Zn–Mg–Cu alloys are closely related to severe coarsening and inefficient reprecipitation of fine strengthening precipitates under the condition of partial precipitation [6]. The thermal cycling in aluminum alloy welding may cause damage to the welding joint [7]. The

weld seam undergoes partial reprecipitation which is dependent upon the cooling rate during the cooling cycle and has determined the final strength [8]. Obvious difference has been observed in the size of MgZn<sub>2</sub> particles ( $\eta$  phase) between the weld seam and the HAZ due to the formation mechanism [8,9]. The cooling rate also varies at different local regions and leads to the difference in local mechanical properties [10]. Al–Zn–Mg–Cu alloys have exhibited high thermal crack sensitivity during arc welding processes because of the Cu element in the alloy. It has been shown by Houldcroft tests that thermal cracks turn up when the Cu content in the high-strength Al–Zn–Mg alloys exceeds 0.8 wt.% [11]. However, Cu element may exist in the form of Al<sub>2</sub>MgCu phase which is a strengthening phase in spray-formed Al–Zn–Mg–Cu alloys [12].

Multi-pass welding has been widely used in welding thick alloy plates, such as the manufacture of pressure vessels and pipes [13]. JONES et al [14] have realized

**Foundation item:** Project (51905126) supported by the National Natural Science Foundation of China; Project (2018M641822) supported by the China Postdoctoral Science Foundation—General Program; Project (HIT.NSRIF.201703) supported by the Natural Scientific Research Innovation Foundation in HIT, China

**Corresponding author:** Yao-hui LÜ; Tel: +86-631-5687027; Fax: +86-631-8641874; E-mail: 3570333103@qq.com  
DOI: 10.1016/S1003-6326(19)65133-2

the welding of 60 mm-thick steel pipe using multi-pass laser welding, and a well-formed weld joint has been obtained. However, the thermal effect of the latter weld seam will strengthen the recrystallization of the former one in multi-pass welding, which may lead to the decrease of mechanical properties [15].

Much work has been done on microstructure and mechanical properties of Al–Zn–Mg–Cu alloy, but little attention has been given to the influence of weld thermal cycle and Cu element on the fracture of multi-pass gas metal arc (GMA) welded Al–Zn–Mg–Cu alloy. In view of this phenomenon, the fracture characteristics and mechanism of this alloy plate were mainly researched.

## 2 Experimental

Self-developed Al–Zn–Mg–Cu alloy plates after T6 heat treatment with the sizes of 100 mm × 50 mm × 20 mm were welded by eight-pass GMA welding, during which ER5356 welding wire was used while argon with purity of 99.99% was chosen as shielding gas. Table 1 shows the nominal chemical compositions of the base metal and welding wire.

**Table 1** Chemical compositions of base metal and welding wire (wt.%)

Alloy	Zn	Mg	Cu	Mn
Base metal	4.5	2.4	0.1	0.25
Welding wire	0.10	4.5–5.5	0.1	0.05–0.2
Alloy	Cr	Ti	Zr	Si
Base metal	0.2	0.08	0.05	≤0.25
Welding wire	0.05–0.2	0.06–0.2		Bal.

The plates were inclined into a V-shape with a U-shape at the bottom, assembled and fixed horizontally according to the size of the groove as shown in Fig. 1. Detailed welding parameters are shown in Table 2.

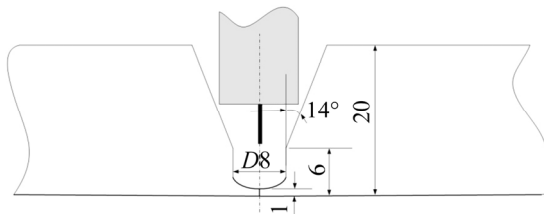


**Fig. 1** Schematic of V-shaped groove with U-shaped bottom (unit: mm)

The macro-morphology of eight-pass welding seams is shown in Fig. 2 [8]. Corrosive liquid is composed of 1 mL HF, 1.5 mL HCl, 2.5 mL HNO<sub>3</sub> and 95 mL deionized water.

**Table 2** Detailed welding parameters of eight weld passes

Weld pass	Weld type	Weld current/A	Weld speed/(m·min <sup>-1</sup> )
1	Rooting weld	240	0.2
2–6	Filling weld	220	0.2
7–8	Capping weld	150	0.2

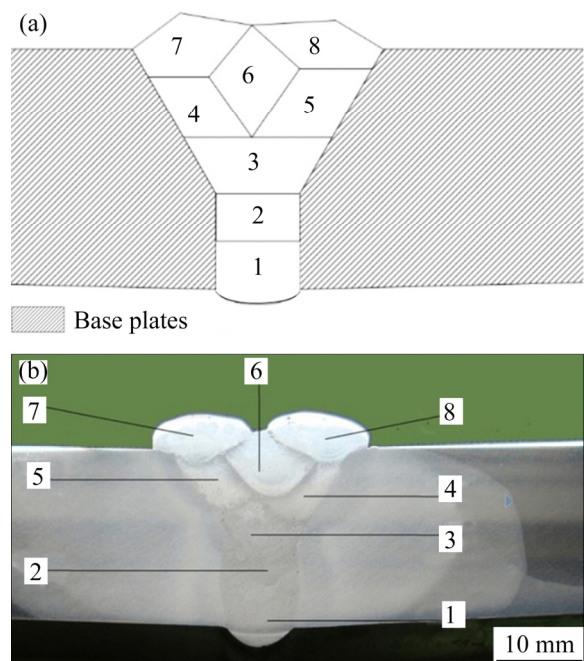


**Fig. 2** Macro-morphologies of eight-pass welding seam: (a) Schematic view; (b) Cross-section [8]

The microstructures and compositions of the base metal and the HAZ were analyzed by SEM (NANOSEM 450) and EDS (Oxford INCA X-ray), respectively. XRD (D/Max 2500, Japan) with Cu K<sub>α</sub> radiation was used to determine the phase composition in HAZ. TEM (JEOL–2100) with an operating voltage of 200 kV and SAED were used to analyze thin foil samples.

Microhardness test was performed along a certain path while the symmetric line in the cross section of the weld joint was made as the reference. Vickers hardness tester was used with the spacing test distance of 0.5 mm, a testing load of 500 g and a loading time of 10 s. The tensile experiment was carried out on a tensile strength tester (MTS808), after which the micromorphology and local chemical composition on the fracture surface of the broken samples were observed by SEM and EDS, respectively. Non-standard tensile specimens numbered as 1 to 5 were taken along the direction perpendicular to the thickness at an interval of 5 mm as shown in Fig. 3. Three samples were fabricated and tested for every numbered zone, in which the tensile strength is the average value of the three samples.

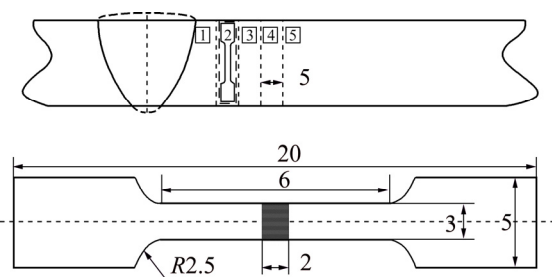


Fig. 3 Schematic of position in HAZ and size of non-standard tensile specimens (unit: mm)

### 3 Results and discussion

#### 3.1 Microstructure of HAZ

The microstructures obtained by SEM are shown in Fig. 4. After the rolling process, solution treatment and artificial aging, the strip microstructures are still retained in the base metal. The strip microstructure gets retained and no equiaxed grains can be found between the strip grains prior to the welding thermal cycle as shown in Fig. 4(e). Figure 4(d) indicates that recrystallization gives birth to equiaxed grains sandwiched by the strip grains in HAZ, which is the most significant difference in microstructural morphology from the base metal. Recrystallization is proved to be gradually weakened by

the gradual reduction of the equiaxed grain area percentage along with the increasing distance to the molten line as shown in Figs. 4(b), (c) and (d). Moreover, the critical position or the border line of recrystallization is 8 mm away from the molten line as shown in Fig. 4(d).

The XRD test and calibration result of the HAZ and the base metal are shown in Fig. 5. The phase composition of the HAZ is identified as  $\alpha(\text{Al}) + \eta(\text{MgZn}_2)$ , while for the base metal it is  $\alpha(\text{Al}) + \eta(\text{MgZn}_2) + \text{Al}_6\text{Mn}$ .

The intragranular and intergranular micro-morphologies of the HAZ by TEM are shown in Figs. 6(a) and (b), respectively. Plenty of nanoscale particles could be intragranularly dispersed including spherical and ellipsoidal particles as shown in Fig. 6(a). The intergranular region is characterized with short rod-like particles and strip precipitates, of which the latter is mainly composed of Al, Zn, Mg and Cu according to the EDS test result as shown in Fig. 6(b). Moreover, the content of Cu in the strip precipitates is remarkably higher than that of the base metal referring to Table 1. The Cu-rich strip precipitates are identified to be  $\text{Al}_2\text{MgCu}$  according to the SAED patterns as shown in Fig. 6(d). Its intergranular distribution in the HAZ is continuous, which might be disadvantageous for the strengthening effect.

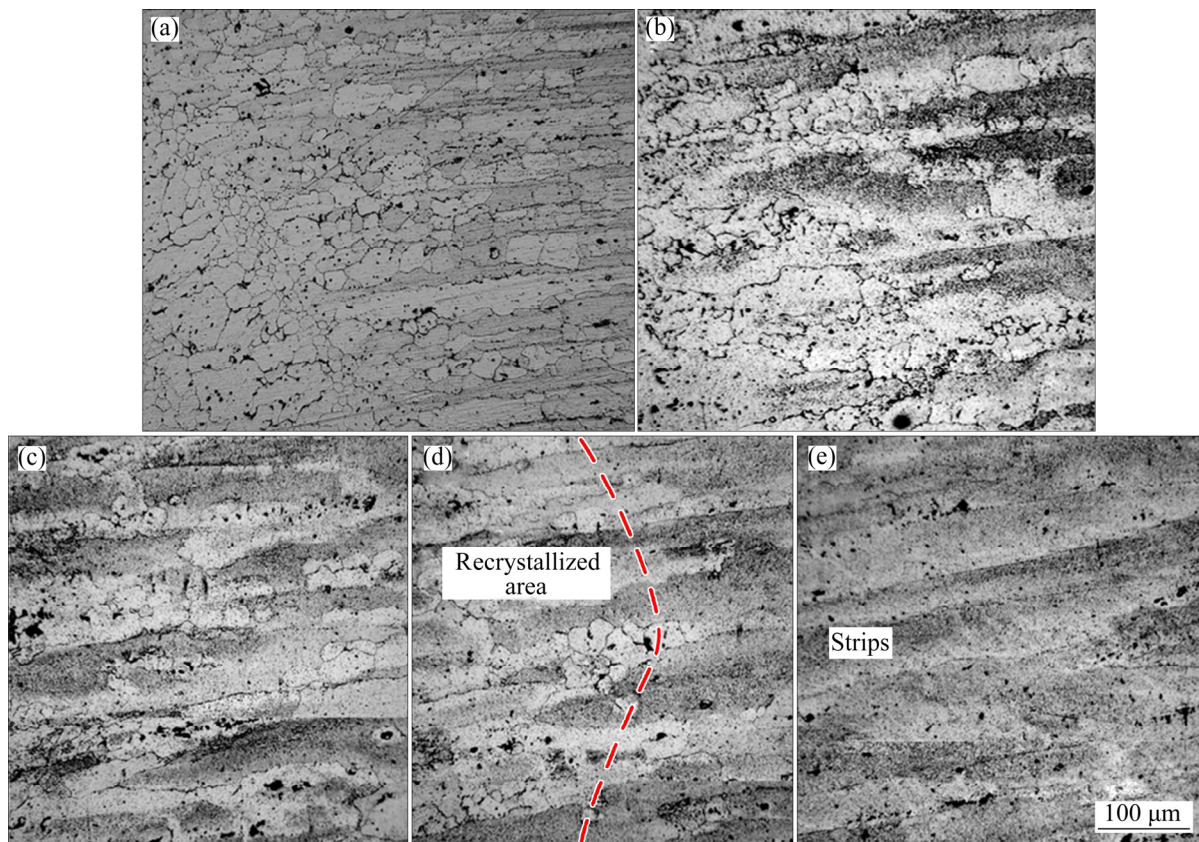


Fig. 4 Microstructures of different local areas with different distances away from molten line: (a) Fusion area; (b) 3 mm; (c) 6 mm; (d) 8 mm; (e) Base metal

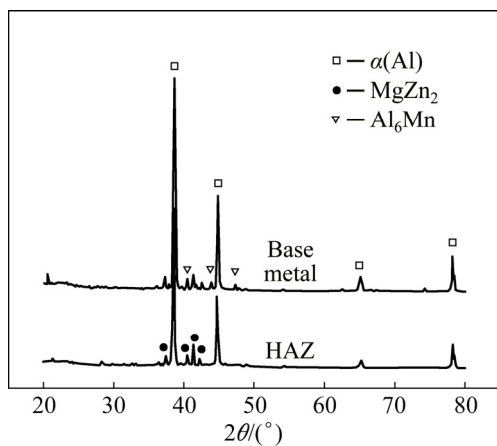


Fig. 5 XRD patterns of HAZ and base metal

### 3.2 Mechanical properties of HAZ

#### 3.2.1 Microhardness

Figure 7 exhibits the distribution of the average microhardness of the three specimens along the path *AC* in multi-pass GMA welded joints. The distribution of microhardness from the weld zone to HAZ is characterized with gradual transition. HAZ has been softened, which is proved by the appearance of most softened zone and the reduced hardness as compared with the base metal. The hardness valley in HAZ is HV 116 and appears in the area about 9 mm away from the center of the weld, or about 1.5 mm away from the molten line.

#### 3.2.2 Tensile strength

Typical ductile fracture has occurred in the weld

seam of the joints during tensile tests along the transverse direction, which has been reported by SHU et al [8]. However, tensile performances of the HAZ along the thickness direction might exhibit obvious differences because microstructure transformation including recovery, recrystallization and precipitation tends to occur in the interface area between the micro strips obtained by the rolling process [16]. The tensile strength of the zone 22.5 mm away from the molten line is equal to that of the base metal as shown in Fig. 8. It is remarkable that the tensile strength of the welded parent material along the thickness direction is lower than 80% of that along the rolling direction. The mechanical properties of the base metal are obviously anisotropic. After the welding thermal cycle, the tensile strength of HAZ along the thickness direction is reduced to 59% of the strength along the rolling direction. The tensile strength of the HAZ firstly decreases and then increases along with the distance away from the molten line, as a result, the valley value of the tensile strength is obtained as the distance is 7.5 mm.

### 3.3 Fracture of HAZ

#### 3.3.1 Morphology and mechanism of fracture

The tensile specimens numbered as 4 and 5 shown in Fig. 3 were used to perform ductile fracture, of which the typical macro morphology of tensile test samples is shown in Fig. 9(a). The fracture surface is composed of numerous dimples with broken particles distributed inside the dimples as shown in Fig. 9(c). Thus, it is proved that obvious plastic deformation and

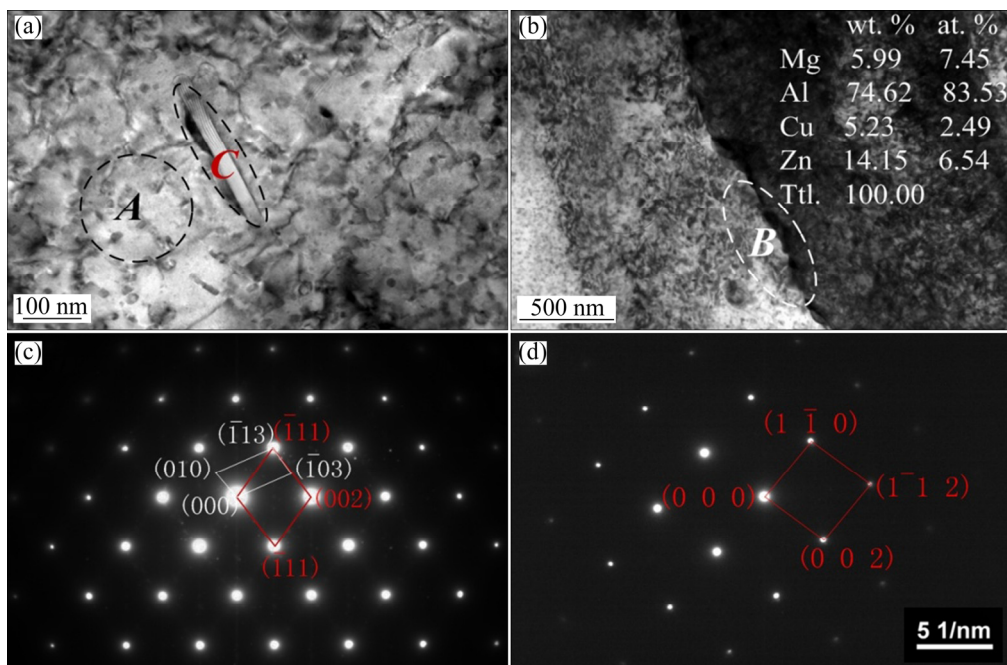


Fig. 6 TEM images (a, b) and SEAD patterns (c, d) of HAZ: (a) Intragranular; (b) Intergranular; (c) [301] zone of  $\text{MgZn}_2$  and [110] zone of  $\alpha(\text{Al})$ ; (d) [011] zone of  $\text{Al}_2\text{MgCu}$

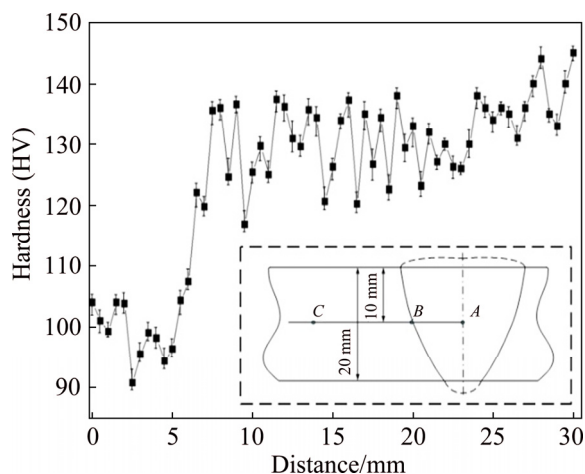


Fig. 7 Microhardness distribution of sample along path AC

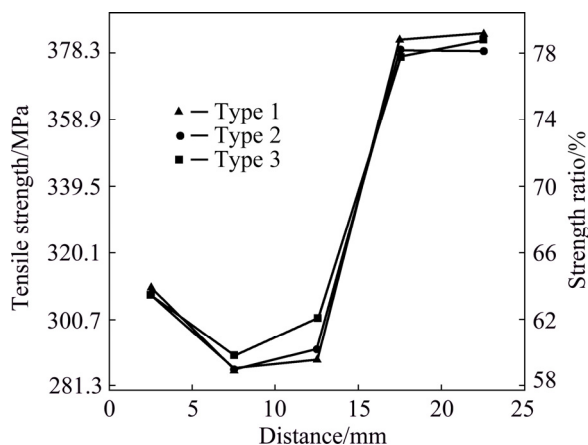


Fig. 8 Tensile strength of samples for different distances away from molten line in HAZ

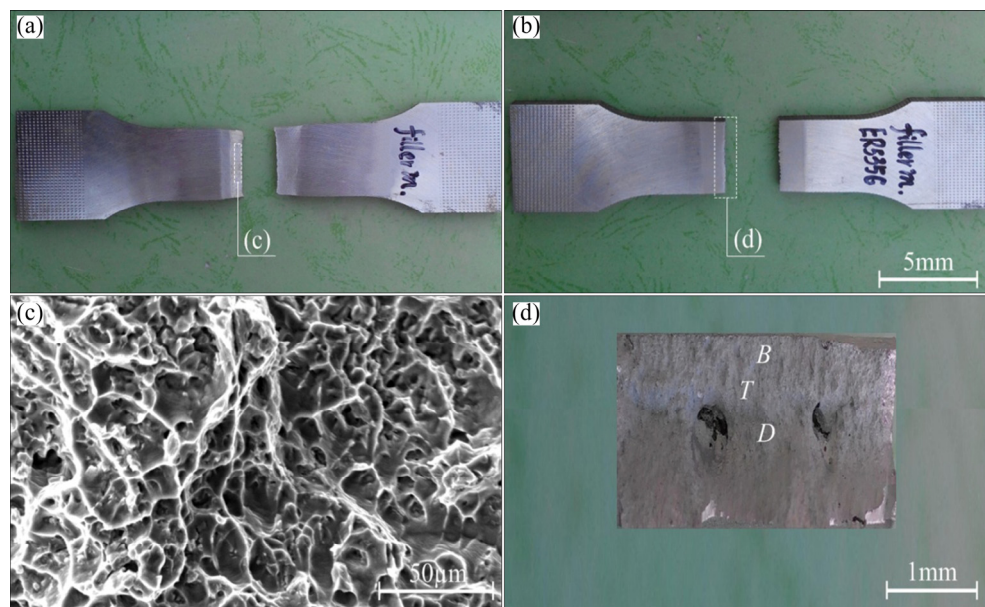


Fig. 9 Typical morphologies of tensile test samples: (a) Typical macromorphology of ductile fracture for tensile specimens numbered 1, 2 and 3 in Fig. 3; (b) Typical macromorphology of brittle fracture for tensile specimens numbered 4 and 5 in Fig. 3; (c) Micromorphology of ductile fracture surface; (d) Macromorphology of ductile/brittle composite fracture surface

strengthening behavior by nano-sized particles occurred before fracture. The typical macroscopic fracture morphology of samples numbered as 1, 2 and 3 in Fig. 3 is shown in Fig. 9(a). Different characteristic regions in the fracture morphology include the ductile fracture region, the brittle fracture region and the transition region between them which are marked as *D*, *B* and *T* in Fig. 9(d), respectively. Thus, the tensile fracture surface in the HAZ is characterized with ductile/brittle composite fracture.

Micromorphologies of *D*, *T* and *B* regions are characterized with high density of dimples, smooth tear plane and fluvial crack propagating path as shown in Figs. 10(a), (b) and (c), respectively. Cu element is mainly distributed along the fluvial cracks according to the EDS test result on the brittle fracture surface as shown in Fig. 10(d), which indicates that the distribution of Cu is favorable for the propagating of cracks during brittle fracture.

### 3.3.2 Influence of Cu element on fracture

Under the condition of T6 heat treatment state, Cu is mainly dissolved in the matrix phase. The content of Cu element in the base metal is no more than 0.2 wt.%. So, it is difficult to find the second phase containing Cu. The second phases containing Cu include CuAl<sub>2</sub> phase and Mg(Zn,Cu)<sub>2</sub> phase. The former precipitation process experiences the enrichment and ordering of Cu atoms, the formation of a transitional phase and the equilibrium phase. Obviously, the process took a long time, whereas the HAZ for welding is unable to provide such heat treatment conditions. The latter is a second phase formed after the substitution of Zn by Cu atoms, as a result, this phase is still present as dispersed particles.

According to the investigation upon microstructure, the Cu-rich phase in the heat affected zone is the  $\text{Al}_2\text{MgCu}$  brittle phase. In addition, the residual stress inside tensile specimens is close to zero. Therefore, the continuous distribution of  $\text{Al}_2\text{MgCu}$  phase in the heat affected zone has played a decisive role and turned the brittle phase into the generation source and propagation path of cracks during the formation and growth process of cracks, respectively, which has promoted the formation of brittle fracture morphology.

### 3.3.3 Micromorphology of precipitated particles

Figure 11 exhibits the micromorphologies of precipitated particles in the base metal, the quenched zone and the over-aged zone. As compared with the base metal, the density and size of precipitated particles in the

quenched zone decrease and slightly increase, respectively, resulting in the consequence that the precipitates are mainly dissolved back to the matrix phase; in addition, the precipitated particles in the over-aged zone are obviously coarsened. As a result, the strengthening effect by precipitated particles should be discounted in the HAZ.

According to the continuous cooling transformation curves of Al–Zn–Mg alloys, the critical cooling rate for the formation of precipitations is between 100 and 110  $^{\circ}\text{C/s}$  as shown in Fig. 12 [17,18]. The base metal has gone through rolling, solid solution treatment and two-stage heat treatment, which leaves a large amount of second phase particles characterized with disperse distribution. In the quenched zone, the HAZ

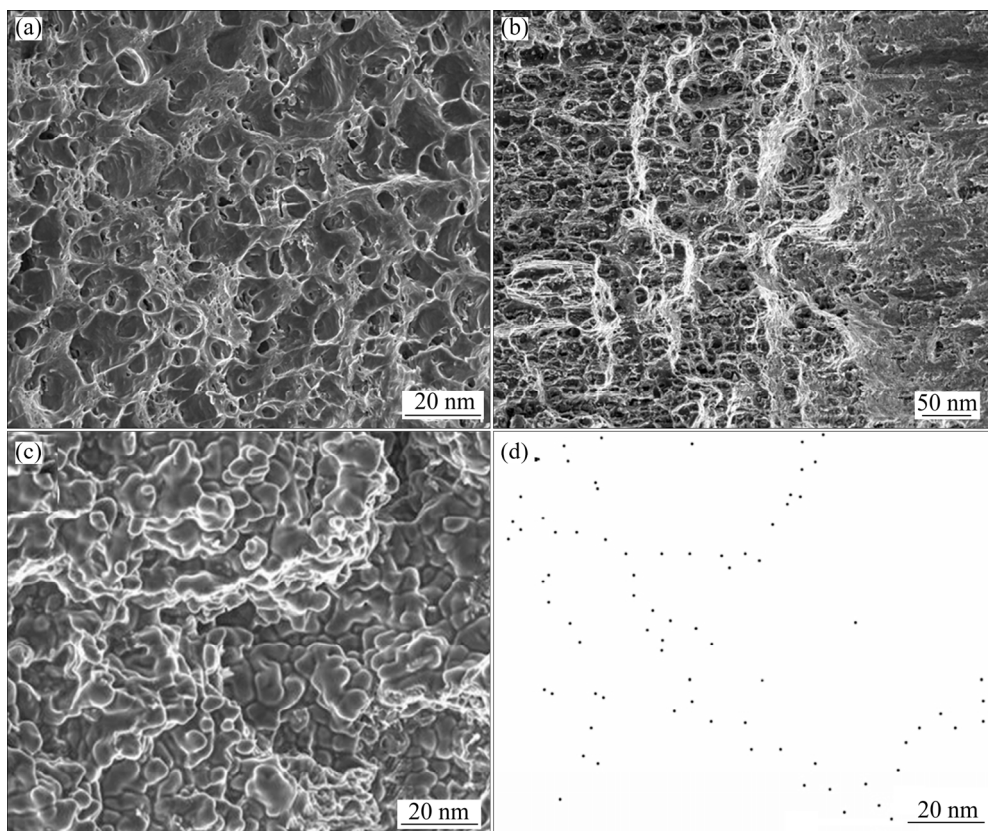


**Fig. 10** Micromorphologies (a, b, c) and local EDS analysis (d) of ductile/brittle composite fracture in different characteristic regions: (a) Ductile fracture region marked as *D* in Fig. 9(d); (b) Transition region marked as *T* in Fig. 9(d); (c) Brittle fracture region marked as *B* in Fig. 9(d); (d) Cu element distribution in brittle fracture region

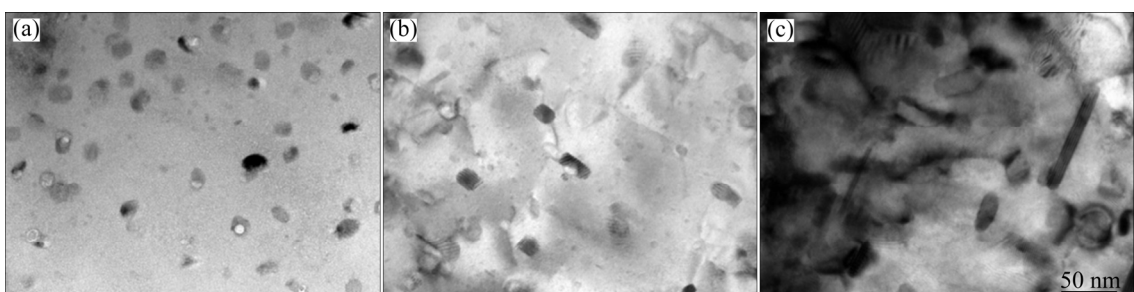


**Fig. 11** Micromorphologies of precipitated particles in substrate plate and HAZ: (a) Base metal; (b) Quenched zone; (c) Over-aged zone

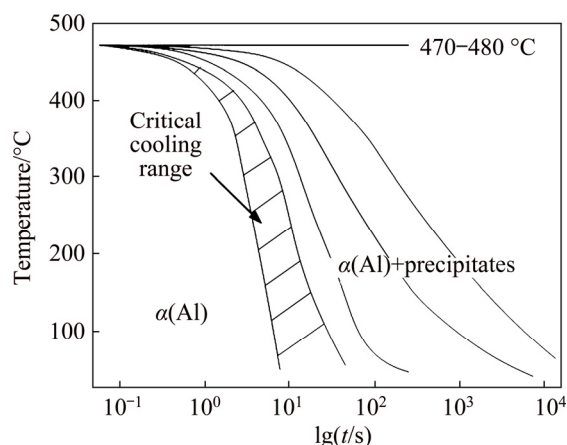


**Fig. 12** Continuous cooling transformation curves of Al-Zn-Mg alloys

re-precipitation of the re-dissolved second phase particles is effectively hindered at the high cooling rate. However, in the over-aged zone of the HAZ the coarsening of second phase particles is actually the result of re-precipitation.

## 4 Conclusions

(1) The percentage of equiaxed grains sandwiched by the strip grains in HAZ gradually decreases along with the increasing distance away from the molten line.

(2) The phase composition of the HAZ is  $\alpha(\text{Al})+\eta(\text{MgZn}_2)$ . Nanoscale particles are intragranularly dispersed while the  $\text{Al}_2\text{MgCu}$  phase is continuously distributed in the strip intergranular precipitates.

(3) The distribution of microhardness is characterized with gradual transition and the hardness valley in HAZ is HV 116. The tensile strength of the HAZ firstly decreases and then increases along with the distance away from the molten line.

(4) The tensile fracture style of HAZ along the thickness direction is ductile/brittle composite fracture and the fracture morphology is composed of the ductile fracture region, the brittle fracture region and the transition region. The feature of these regions is high density of dimples, smooth tear plane and fluvial crack propagating path.

(5) The continuous distribution of  $\text{Al}_2\text{MgCu}$  phase is responsible for the generation and propagating of cracks during brittle fracture. The precipitated particles coarsen in the quenched and over-aged zones, causing the deterioration of mechanical properties of the HAZ.

## References

[1] YAN Zhong-jie, LIU Xue-song, FANG Hong-yuan. Effect of sheet configuration on microstructure and mechanical behaviors of

dissimilar Al-Mg-Si/Al-Zn-Mg aluminum alloys friction stir welding joints [J]. Journal of Materials Science & Technology, 2016, 32(12): 1378–1385.

[2] LEI Chao, YANG He, LI Heng, SHI Nian, FU Jin, ZHAN Li-hua. Dependence of creep age formability on initial temper of an Al-Zn-Mg-Cu alloy [J]. Chinese Journal of Aeronautics, 2016, 29(5): 1445–1454.

[3] KOMARASAMY M, ALAGARSAMY K, ELY L, MISHRA R S. Characterization of 3" through-thickness friction stir welded 7050-T7451 Al alloy [J]. Materials Science and Engineering A, 2018, 716: 55–62.

[4] UMAMAHESHWER RAO A C, VASU V, GOVINDARAJU M, SAI SRINADH K V. Stress corrosion cracking behaviour of 7xxx aluminum alloys: A literature review [J]. Transactions of Nonferrous Metals Society of China, 2016, 26(6): 1447–1471.

[5] LIAO Yu-guo, HAN Xiao-qi, ZENG Miao-xia, JIN Man. Influence of Cu on microstructure and tensile properties of 7xxx series aluminum alloy [J]. Materials and Design, 2015, 66: 581–586.

[6] WANG Xi-ling. Study on TIG welding process and properties of 7xxx series aluminum alloy by spray forming [D]. Zhenjiang: Jiangsu University of Science and Technology, 2011: 53–61. (in Chinese)

[7] MI Guo-fa, ZHAO Da-wei, DONG Cui-fen, NIU Ji-tai, JIN Cheng. Void damage evolution of LF6 aluminum alloy welded joints under external load and thermal cycling conditions [J]. Transactions of Nonferrous Metals Society of China, 2010, 20(10): 1968–1973.

[8] SHU Feng-yuan, SUN Yi-ming, ZHAO Hong-yun, SONG Xiao-guo, SUI Shao-hua, HE Wen-xiong, HE Peng, LIU Bin, XU Bin-shi. Microstructural and mechanical inhomogeneity in the narrow-gap weld seam of thick GMA welded Al-Zn-Mg alloy plates [J]. Journal of Materials Research, 2016, 31(24): 3948–3955.

[9] ENTESARI S, ABDOLLAH-ZADEH A, HABIBI N, MEHRI A. Experimental and numerical investigations into the failure mechanisms of friction stir welded AA7075-T6 thin sheets [J]. Journal of Manufacturing Processes, 2017, 29: 74–84.

[10] ROUT P K, GHOSH K S. Effect of microstructural features on stress corrosion cracking behaviour of 7017 and 7150 aluminium alloy [J]. Materials Today: Proceedings, 2018, 5(1): 2391–2400.

[11] ZHANG Liang, LI Xiao-yuan, NIE Zuo-ren, HUANG Hui, NIU Lan-qiang. Comparison of microstructure and mechanical properties of TIG and laser welding joints of a new Al-Zn-Mg-Cu alloy [J]. Materials & Design, 2016, 92: 880–887.

[12] LI Yong-bing, HUANG Jin-feng, CUI Hua, CAI Yuan-hua, ZHANG Kui, ZHANG Ji-shan. Microstructure evolution of spray-formed Mg-9Al-xZn alloys [J]. Transactions of Nonferrous Metals Society of China, 2009, 19(7): 1189–1196.

[13] FENG Jie-cai, GUO Wei, IRVINE N, LI Lin. Understanding and elimination of process defects in narrow gap multi-pass fiber laser welding of ferritic steel sheets of 30 mm thickness [J]. The International Journal of Advanced Manufacturing Technology, 2017, 88(5–8): 1821–1830.

[14] JONES L P, AUBERT P, AVILOV V, COSTE F, DAENNER W, JOKINEN T, NIGHTINGALE K R, WYKES M. Towards advanced welding methods for the ITER vacuum vessel sectors [J]. Fusion Engineering & Design, 2003, 69(1): 215–220.

[15] WANG Bo-ping, ZHAO Yong, HUANG Jian. Investigation on microstructure of thick plate stainless steel joint welded by multi-pass laser welding with filler wire [J]. China Laser, 2013, 40(2): 122–126.

[16] ZHANG K, CHEN J Q, MA P Z, ZHANG X H. Effect of welding thermal cycle on microstructural evolution of Al-Zn-Mg-Cu alloy

[17] GANCARZ T, JOURDAN J, GASIOR W, HENEIN H. Physicochemical properties of Al, Al–Mg and Al–Mg–Zn alloys [J]. Journal of Molecular Liquids, 2018, 249: 470–476.

[18] CHEN Gao-jin, CHEN Liang, ZHAO Guo-qun, ZHANG Cun-sheng. Microstructure evolution during solution treatment of extruded Al–Zn–Mg profile containing a longitudinal weld seam [J]. Journal of Alloys and Compounds, 2017, 729(30): 210–221.

## 多道熔化极气体保护焊 Al–Zn–Mg–Cu 合金热影响区的组织和力学性能

周佳良<sup>1</sup>, 舒凤远<sup>1</sup>, 赵洪运<sup>1</sup>, 吕耀辉<sup>2</sup>, 刘玉欣<sup>2</sup>, 何鹏<sup>3</sup>

1. 哈尔滨工业大学(威海) 山东省特种焊接技术重点实验室, 威海 264209;
2. 国家再制造重点实验室, 北京 100072;
3. 哈尔滨工业大学 先进焊接与连接国家重点实验室, 哈尔滨 150001

**摘要:** 研究多道熔化极气体保护焊 Al–Zn–Mg–Cu 合金板中热影响区的组织和力学性能, 在此基础上分析热影响区的力学各向异性的形成和断裂机理。采用扫描电镜(SEM)和能谱仪(EDS)对其显微组织和组成进行分析。采用 X 射线衍射仪(XRD)、透射电子显微镜(TEM)和选择性区域电子衍射仪(SAED)分析相组成。显微硬度的分布特征是逐渐过渡的, 而抗拉强度有先减小后增大的趋势。在  $\alpha$ (Al)中的纳米级  $\eta$ (MgZn<sub>2</sub>)粒子和 Al<sub>2</sub>MgCu 相的分布决定沿厚度方向的拉伸性能并导致形成的热影响区韧性/脆性复合断裂。在带状析出物晶间连续分布的 Al<sub>2</sub>MgCu 相导致早期裂纹和脆性断裂区域的形成, 粗化的析出粒子也导致力学性能的恶化。

**关键词:** Al–Zn–Mg–Cu 合金; 热影响区; 显微组织; 力学性能; 韧性/脆性复合断裂

(Edited by Xiang-qun LI)